

FINAL REPORT

Low-Cost Ultra-Wideband EM Sensor for UXO Detection and Classification

SERDP Project MR-2105

APRIL 2012

Charles P. Oden
Earth Science Systems, LLC

This document has been cleared for public release



REPORT DOCUMENTATION PAGE				Form Approved OMB No. 0704-0188	
<p>The public reporting burden for this collection of information is estimated to average 1 hour per response, including the time for reviewing instructions, searching existing data sources, gathering and maintaining the data needed, and completing and reviewing the collection of information. Send comments regarding this burden estimate or any other aspect of this collection of information, including suggestions for reducing the burden, to the Department of Defense, Executive Services and Communications Directorate (0704-0188). Respondents should be aware that notwithstanding any other provision of law, no person shall be subject to any penalty for failing to comply with a collection of information if it does not display a currently valid OMB control number.</p> <p>PLEASE DO NOT RETURN YOUR FORM TO THE ABOVE ORGANIZATION.</p>					
1. REPORT DATE (DD-MM-YYYY) 08-03-2012		2. REPORT TYPE Final Report		3. DATES COVERED (From - To) April 2011-April 2012	
4. TITLE AND SUBTITLE Compact Low-Cost Ultra-Wideband EMI Sensor for UXO Detection and Classification				5a. CONTRACT NUMBER W912HQ-11-C-0037	
				5b. GRANT NUMBER	
				5c. PROGRAM ELEMENT NUMBER	
6. AUTHOR(S) Charles P. Oden				5d. PROJECT NUMBER SERDP MR-2105	
				5e. TASK NUMBER	
				5f. WORK UNIT NUMBER	
7. PERFORMING ORGANIZATION NAME(S) AND ADDRESS(ES) Earth Science Systems, LLC 11485 W. I-70 Frontage Rd., Unit B Wheat Ridge, CO 80033				8. PERFORMING ORGANIZATION REPORT NUMBER	
9. SPONSORING/MONITORING AGENCY NAME(S) AND ADDRESS(ES) Strategic Environmental Research and Development Program 901 NORTH STUART STREET SUITE 303 ARLINGTON VA 22203				10. SPONSOR/MONITOR'S ACRONYM(S) SERDP	
				11. SPONSOR/MONITOR'S REPORT NUMBER(S)	
12. DISTRIBUTION/AVAILABILITY STATEMENT Approved for public release; distribution is unlimited.					
13. SUPPLEMENTARY NOTES					
14. ABSTRACT <p>This SERDP SEED project investigated the viability of using low-cost commercially available magneto-resistive sensors for EM induction and magnetometry. Because there are many different configurations for operating these sensors, a custom circuit board was designed and fabricated to determine which configuration would be most optimal for UXO detection and discrimination.</p> <p>Noise and sensitivity measurements were conducted in the frequency domain using a Helmholtz coil. Magnetic biasing, electrical bridge biasing, chopper techniques, and open/closed loop configurations were investigated. The optimal configuration produced a noise density of 6 pT/√Hz for frequencies above 200 Hz. At 1 Hz, the noise density is ~ 30 pT/√Hz. These results were obtained in both open loop and closed loop operation.</p> <p>A laboratory prototype instrument was built using the magneto-resistive sensors to test the magnetometer and EM induction response to actual UXO targets and compare with readings from similar instruments. When operating in magnetometer mode, the prototype detected an 81 mm target at a distance of over two meters. When operating in time-domain EM induction mode, measurements could be made as early as 20 μs after the transmitter turn-off.</p>					
15. SUBJECT TERMS UXO, Ordnance, Magneto-resistor, Induction, Magnetometer					
16. SECURITY CLASSIFICATION OF:			17. LIMITATION OF ABSTRACT None	18. NUMBER OF PAGES 31	19a. NAME OF RESPONSIBLE PERSON Charles P. Oden
a. REPORT None	b. ABSTRACT None	c. THIS PAGE None			19b. TELEPHONE NUMBER (Include area code) 303-800-2000

Table of Contents

1	Abstract.....	1
2	Objective.....	2
3	Background	2
4	Materials and Methods	5
5	Results and Discussion	10
5.1	DC Biased AMR Noise Density	11
5.2	DC Biased AMR Noise Density Using a Flux Concentrator.....	12
5.3	AC Biased AMR Noise Density Using a Flux Concentrator.....	13
5.4	Issues with Flux Concentrators.....	13
5.5	Advanced Magnetic Biasing Techniques	13
5.6	EMI Response to an 81 mm UXO	14
5.7	Magnetometer Response to an 81 mm UXO	18
5.8	Response to a 25 mm Target.....	18
5.9	Sensor Calibration and Drift.....	19
6	Conclusions and Implications for Future Research	20
7	Literature Cited.....	23

List of Figures

Figure 1. Diagram of an AMR sensor (adapted from Honeywell AMR sensor datasheet).	4
Figure 2: Block diagram of the MR sensor signal processing system.	5
Figure 3. Photograph of the prototype AMR sensor board. The AMR sensor chip is circled.	6
Figure 4. Photograph of the digital signal processing system with a PC and the MOTU digital audio unit (left). Photograph of the MOTU digital audio unit and signal cables that connect to the prototype sensor board (right).	7
Figure 5. Photograph of the sensor board placed in the Helmholtz coil (left) and being lowered into a triple layered magnetic shield. Photograph of the sensor and Helmholtz coil installed inside the magnetic shield (right).	8
Figure 6. Photograph of a bench-top TD EMI system with the transmitter coil visible and an 81 mm mortar (left). Photograph of the AMR sensor board and the transmitter board inside the transmitter coil form (right).	9
Figure 7. Photograph of pickup coil used to monitor the transmitted signal from the bench-top time-domain EMI system (left). Oscilloscope screen capture of the early-time AMR sensor response (right). The transmitted signal received by the monitoring coil is shown in yellow, and the raw received signal from the AMR sensor is shown in green.	10
Figure 8. The noise spectrum of the AMR prototype system with the AMR sensor output shorted (left). The noise spectrum of the AMR prototype system with the AMR sensor output shorted and using a modulator to shift the LNA noise out of band (left).	11
Figure 9. The noise spectrum of the AMR prototype system with no feedback (left). The noise spectrum of the system when using magnetic feedback (right).	12
Figure 10. The AMR sensor with flux concentrators installed (left). The noise density results using a DC bridge current and flux concentrators (right).	12
Figure 11. The AMR sensor noise density results using a DC bridge current and flux concentrators.	13
Figure 12. Stoner-Wohlfart asteroid (left) and AMR hysteresis curve (right). Adapted from Tumanski (2001).	14
Figure 13. Photograph of an 81mm mortar.	15
Figure 14. ALLTEM profile data for an 81 mm target at 310 μ s. The target was 44.4 cm below the ALLTEM sensor cube. Adapted from Asch (2011).	15
Figure 15. EMI Response to an 81 mm mortar. The left panels shows a linear single decay curve plot with the ordnance at the - 9 cm position. The right panel shows the same data on a logarithmic plot.	16
Figure 16. The left panel shows the decay curves as a function of position. The right panel shows transients at the indicated time versus ordnance position.	16
Figure 17. Illustration of magnetometer test setup.	17
Figure 18. Magnetic response of the 81 mm target.	18
Figure 19. Photograph of a 25 mm target.	18
Figure 20. EMI Response of 25 mm target.	19
Figure 21. Left panel shows the drift of the negative AMR sensor output as the permalloy magnetization is reversed (blue). The green curve is the average response. The center panel shows the data for the positive AMR sensor output. The right panel is the	

compensated response, which is the sum of the green traces in the previous panels. After compensation, the drift is about 1% of the uncompensated drift.....	20
Figure 22. Photograph of an ESS designed ground penetrating radar system. The small size of these electronics illustrates ESS's capabilities in designing optimal electronic solutions using the latest technologies.	21

List of Tables

Table 1. List of magnetic sensor types and their associated noise densities.....	4
Table 2. Transmitter moments of common EMI instruments.....	9

List of Acronyms

1-C	One Component (receiver)
3-C	Three Component (receiver)
2-D	Two Dimensional
AC	Alternating Current
ADC	Analog to Digital Converter
AMR	Anisotropic magneto-resistance
COTS	Commercial-Off-The-Shelf
DAC	Digital to Analog Converter
DC	Direct Current
DSP	Digital Signal Processor
EM	Electromagnetic
EMI	Electromagnetic Induction
ESS	Earth Science Systems, LLC
ESTCP	Environmental Security Technology Certification Program
FFT	Fast Fourier Transform
FPGA	Field Programmable Gate Array
GPS	Global Positioning System
IC	Integrated Circuit
IMU	Inertial Measurement Unit
MEMS	Micro-Electrical-Mechanical System
MOTU	Mark of the Unicorn – a brand name for audio equipment
MR	Magneto-Resistance
NIST	National Institute of Standards and Technology
RTK	Real-Time Kinematic
SERDP	Strategic Environmental Research and Development Program
SPS	Samples Per Second
SNR	Signal to Noise Ratio
USGS	United States Geological Survey
UXO	Unexploded Ordnance

Keywords

Unexploded Ordnance, EM Induction, Magneto-resistor, Magnetometer

Acknowledgements

This work was supported by the Strategic Environmental Research and Development Program Project MR-2105.

1 Abstract

This SERDP SEED project investigated the viability of using low-cost commercially available magneto-resistive sensors for EM induction and magnetometry. Because there are many different configurations for operating these sensors, a custom circuit board was designed and fabricated to determine which configuration would be most optimal for UXO detection and discrimination.

Noise and sensitivity measurements were conducted in the frequency domain using a Helmholtz coil. Magnetic biasing, electrical bridge biasing, chopper techniques, and open/closed loop configurations were investigated. The optimal configuration produced a noise density of 6 pT/ $\sqrt{\text{Hz}}$ for frequencies above 200 Hz. At 1 Hz, the noise density is ~ 30 pT/ $\sqrt{\text{Hz}}$. These results were obtained in both open loop and closed loop operation.

A laboratory prototype instrument was built using the magneto-resistive sensors to test the magnetometer and EM induction response to actual UXO targets and compare it with readings from similar instruments. When operating in magnetometer mode, the prototype detected an 81 mm target at a distance of over two meters. When operating in time-domain EM induction mode, measurements could be made as early as 20 μs after the transmitter turn-off. Instruments using coils as receivers typically can only receive signals after 100 μs . The induced currents at early-time provide more information about the shape of the target than the late-time currents. Furthermore, the small size of the magneto-resistive sensor does not spatially average the received signal like a large coil does. These sensor attributes provide more information for discrimination than conventional EM induction instruments.

The results of this investigation show that a man-portable instrument similar in physical configuration to the metal detectors commonly used by the public on beaches can be built for UXO detection and discrimination. The instrument can be operated as both a magnetometer to detect targets and in EM induction mode for discrimination. The small size and low-cost enables the production of portable array systems with many receivers that are similar to the ‘advanced’ discrimination systems available such as the MetalMapper.

2 Objective

The objective of this SERDP SEED project is to show that magneto-resistive sensors are suitable for use in EM induction and magnetometer instruments for UXO detection and discrimination. The noise and sensitivity measurements made for this project will provide benchmarks for comparison with commonly used instruments for UXO detection and classification. The goal and metric for success is to build a MR sensor with sensitivity that approaches that of high-quality flux-gate magnetometers (less than 10 pT/ $\sqrt{\text{Hz}}$).

A laboratory prototype EM induction and magnetometer instrument was built so that a simple capabilities demonstration could be conducted. Due to the limited scope of a SEED project, only basic experiments were conducted. The goal for these demonstrations is to show that magneto-resistive sensors have sufficient sensitivity for both EM induction surveys for UXO discrimination and for UXO detection using magnetometry.

The experiments performed during this project show that magneto-resistive sensors are suitable for use in ‘advanced’ (i.e. multiple transmitter multiple receiver) man-portable instruments. These sensors enable the construction of instruments that are lighter, more maneuverable, less-expensive, and provides a richer dataset than existing man-portable equipment. Man-portable instruments with magneto-resistive sensors can perform both EM induction and magnetometer measurements in a wide variety of terrain and vegetation conditions.

This project addresses SERDP’s Statement of Need MMSEED-11-01, which states that sensors technology is needed that can be adapted to a wide range of deployment methods (hand held, airborne, cart based, etc.), that can provide data to aid in classification of a mix of munition types in close proximity, and that can operate in high clutter or otherwise noisy environments.

3 Background

Geophysical surveys for UXO detection utilize both magnetometer and EMI measurements. EMI measurements are not generally able to detect targets to the same depth that magnetometer measurements can. This is because the EMI primary source field attenuates with distance from the transmitter (approximately at $1/r^3$) and the secondary induced field from the target also attenuates with distance from the target (approximately at $1/r^3$), which results in two-way attenuation. Conversely, the passive magnetic fields due to the targets are only attenuated with distance from the source (approximately at $1/r^3$), which results in one-way attenuation. Measurements from ‘advanced’ EMI systems with many transmitting and receiving coils (e.g., the MetalMapper) provide more information about the size, shape, and identity of the target. As a result, two geophysical surveys are commonly employed at UXO remediation sites: one with a sensitive instrument for detection purposes, and another with many sensors for characterization and classification purposes.

The current state of the practice involves cart-based sensors that are either pushed by hand or towed by a tractor. This arrangement works well for smooth and open field sites, but is not well suited for sites with rough topography or significant vegetation (e.g., a forest). For these more challenging sites, newly developed hand-held sensors are used. The current generation of hand-held sensors being tested includes the Bud-Lite, the MPV, and the 2x2 TEMTADS. All of

these systems are bulky and rather unwieldy. Some systems require a second person to carry a backpack with electronic gear. A maneuverable and lightweight sensor such as the metal detectors used by ‘beach combers’ is more desirable.

One reason for building ‘advanced’ instruments with many receivers is that the sensors can be mounted on a rigid platform so that the attitude and position (relative to each other) is precisely known. This allows a single statically acquired (i.e. instrument held stationary) ‘snapshot’ to be taken to analyze a single target. Instruments with fewer coils can be used to collect datasets with similar spatial coverage, but uncertainties in position measurements often make this method’s performance subpar. For example, the typical uncertainties from RTK GPS measurement are typically a few cm. Promising research using laser systems and IMU system has been conducted by (Barrow et al., 2006, Foley et al. 2008) for attaining the sub-centimeter positional uncertainties needed for dynamic surveys. Upcoming navigation methods under development at ESS include UWB radar ranging and optically aided inertial measurements. The salient point is that several navigation technologies are rapidly developing that have the required sub-centimeter positioning uncertainties needed for dynamic surveys. With the positioning problem (soon to be) solved, the remaining need is for miniaturized sensors so that ‘advanced’ man-portable instruments can be made for conducting dynamic surveys for both detection and discrimination.

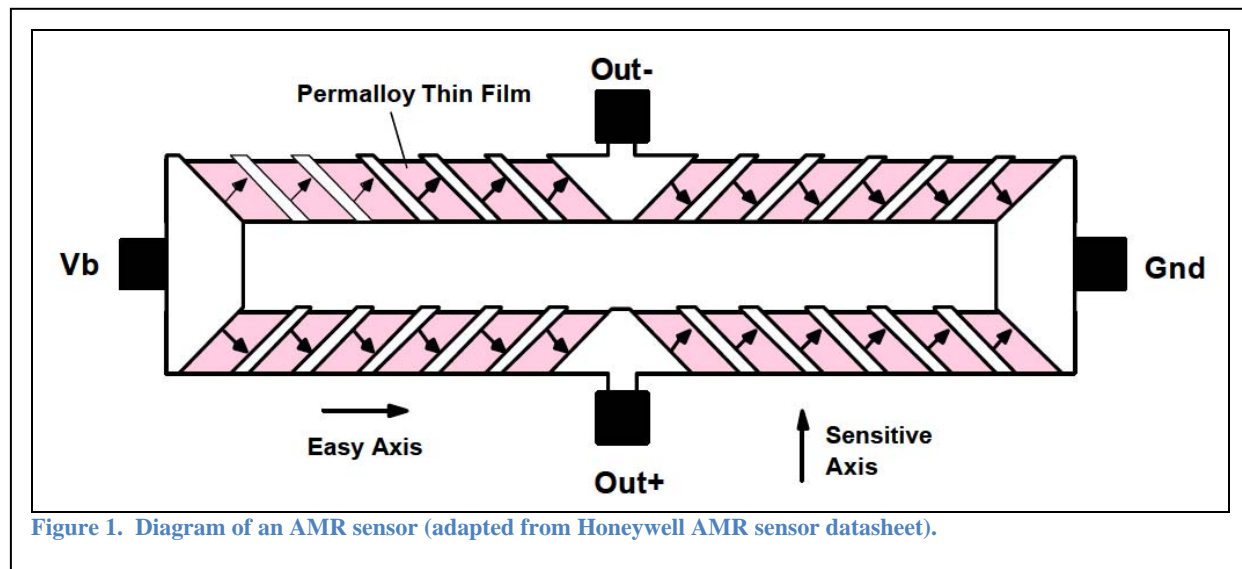
Historically, the reason that MR sensors were not been used for metal detectors is that they were too noisy. Although there are many varieties of MR devices, most commercially available sensors are one of three types: giant magneto-resistance (GMR) devices, tunneling magneto-resistance (TMR) devices, and anisotropic magneto-resistance (AMR) devices. These devices are usually supplied in the Wheatstone bridge configuration, which measures a single component of the magnetic field in a specified direction. Although GMR and TMR sensors are more sensitive, AMR sensors have the lowest noise at low frequencies and are preferred for low-field sensing. The noise density of an instrument is primarily determined by both the noise density of the sensor and the noise density of the first amplifier. The magnetic field sensors most commonly used for UXO work are magnetometers and induction coils. Flux gates are the most common magnetometer used, but proton and Overhauser magnetometers are also used. Table 1 lists typical noise densities for these instruments. The flux coil noise density listed is the best possible achieved value calculated using formulas from Tumanski (2007), and do not include the noise contribution for the electronics amplifiers. Many of the magnetometers listed do not have sufficient bandwidth for EMI measurements.

Induction coils have demonstrated high sensitivity to time varying fields. The SNR of a coil increases with the square of its diameter, and the square root of the number of turns (Tumanski, 2007). Unfortunately, increasing the size of the coil reduces its spatial resolution, and increasing the number of turns increases its inductance making early-time operation difficult with time-domain measurements. Using the formulas given in Tumanski (2007), an induction coil having approximately the same size as an AMR sensor (3 cm diameter with 100 turns) has noise density of $1.2 \text{ pT}/\sqrt{\text{Hz}}$ at 1 kHz. For reference, the Metal Mapper uses 10 cm square receiver coils and has a stated noise density of $4 \text{ nT}/\sqrt{\text{Hz}}$ (this includes noise generated by the electronics).

Magnetic noise in the environment may raise the effective noise floor. For example, Schumann resonance typically has a noise density of $10\text{-}20 \text{ pT}/\sqrt{\text{Hz}}$ (Bianchi and Meloni, 2007). Manmade noise sources can be much larger (power distribution systems, etc.). Noise due to vibrations and movement of the sensor in the earth’s magnetic field are also significant.

Table 1. List of magnetic sensor types and their associated noise densities.

Sensor Type	Noise Density	Sensor Bandwidth	Information Source
Flux gate vector mag.	6 - 10 pT/ $\sqrt{\text{Hz}}$ at 1 Hz	1 kHz typ.	Bartington Mag-03 documentation
Search coil (1 turn, 1 m diameter)	6.2 fT/ $\sqrt{\text{Hz}}$ at 1 kHz 6.2 pT/ $\sqrt{\text{Hz}}$ at 1 Hz		Tumanski (2007) formulation
MetalMapper receiver coil	4 nT/s- $\sqrt{\text{Hz}}$ 4 pT/ $\sqrt{\text{Hz}}$ @ 1 kHz 4 nT/ $\sqrt{\text{Hz}}$ @ 1 Hz	10 kHz	Geometrics sales literature
Overhauser total field mag.	22 pT/ $\sqrt{\text{Hz}}$	60 Hz	GEM Systems documentation
Proton total field mag.	150 pT at 1 Hz	1 Hz	GEM Systems documentation
Optically pumped mag.	2.5 pT at 1 Hz	20 Hz	GEM Systems documentation
AMR sensor	31 pT/ $\sqrt{\text{Hz}}$ @ 200 Hz	DC to >100 kHz	This study
AMR sensor with flux concentrator	30 pT/ $\sqrt{\text{Hz}}$ @ 1 Hz 6 pT/ $\sqrt{\text{Hz}}$ @ 200 Hz	DC to > 100 kHz	This study

**Figure 1. Diagram of an AMR sensor (adapted from Honeywell AMR sensor datasheet).**

Several researchers and groups have examined MR sensors for geophysical applications and some have built prototype instruments, including Chaiken (1996), Dalichaouch et al. (2001), Dalichaouch and Czipott (2007), and Oden et al. (2008, see Figure 3). Additionally, several organizations have worked in this area but have not published their work, including Geometrics

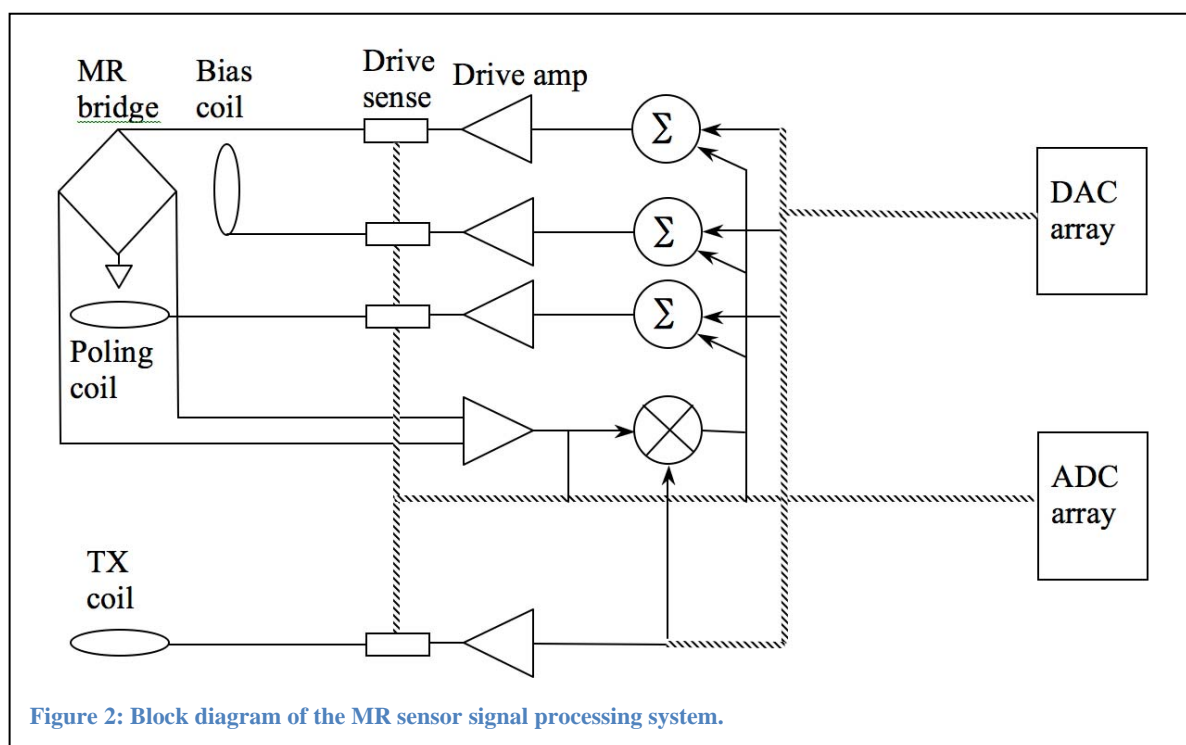
(Mark Prouty, pers. comm.), Auburn University (Lloyd Riggs, pers. comm.), and Blackhawk (Bob Grimm, pers. comm.). Dalichaouch is the only researcher from this list that has developed an active EMI system using AMR sensors. Despite these previous efforts, research in MR phenomenon continues at a fast pace. There are many methods for operating these devices that result in improved performance, and many have not yet been implemented into geophysical instruments.

AMR sensors are comprised of a permalloy film with overlying copper strips that guide electrical currents in a preferential direction through the film (see Figure 1). They are usually built in a Wheatstone bridge configuration. The resistance of the sensor is a function of the angle between the magnetization direction (i.e., the easy axis) and the direction of current flow (arrows at 45 degrees from the easy axis in Figure 1). As the magnetic field along the sensitive axis changes, the magnetization in the permalloy film rotates about the easy axis, which changes the resistance of the sensor. Figure 1 shows the conventional and most stable method of operation, however rotating the magnetization to other directions such as the sensitive axis can provide more sensitivity (Tumaski, 2001). These ‘alternative’ methods of biasing are typically unstable and bring practical difficulties. Experimental results examining these ‘alternative’ methods are given in the Results and Discussion section.

Other notable magnetometer technologies that should see commercialization in the near future include the giant magneto-impedance effect (not to be confused with the giant magnetoresistance effect) and TMR devices. Sensitive magnetometers have also been built using Bose-Einstein condensates.

4 Materials and Methods

A custom prototype sensor circuit board was constructed to test and evaluate the various operating modes of the AMR sensors. The sensor electronics were designed around an HMC1002 AMR sensor from Honeywell, and a MOTU digital signal processing system for



generating and recording arbitrary waveforms. The AMR sensor is a resistor network in a Wheatstone bridge configuration. Very high quality low-noise amplifiers (LNAs) were used to amplify the signal produced by the AMR sensor. The AMR sensor has a noise density of $29 \text{ nV}/\sqrt{\text{Hz}}$ and the LNAs have a noise density of $1.1 \text{ nV}/\sqrt{\text{Hz}}$. Circuits were provided to drive the bridge with both DC and AC excitations generated by the signal processing system. The AMR sensor chip has integrated coils for setting the magnetic state of the sensor element and to add a bias magnetic field. Circuits were implemented to excite both of these coils with arbitrary DC and/or AC signals. Finally, circuits were implemented to modulate and demodulate both magnetic and electronic analog signals associated with the sensor operation. A block diagram of the system is shown in Figure 2 and a photograph of the prototype sensor board is shown in Figure 3.

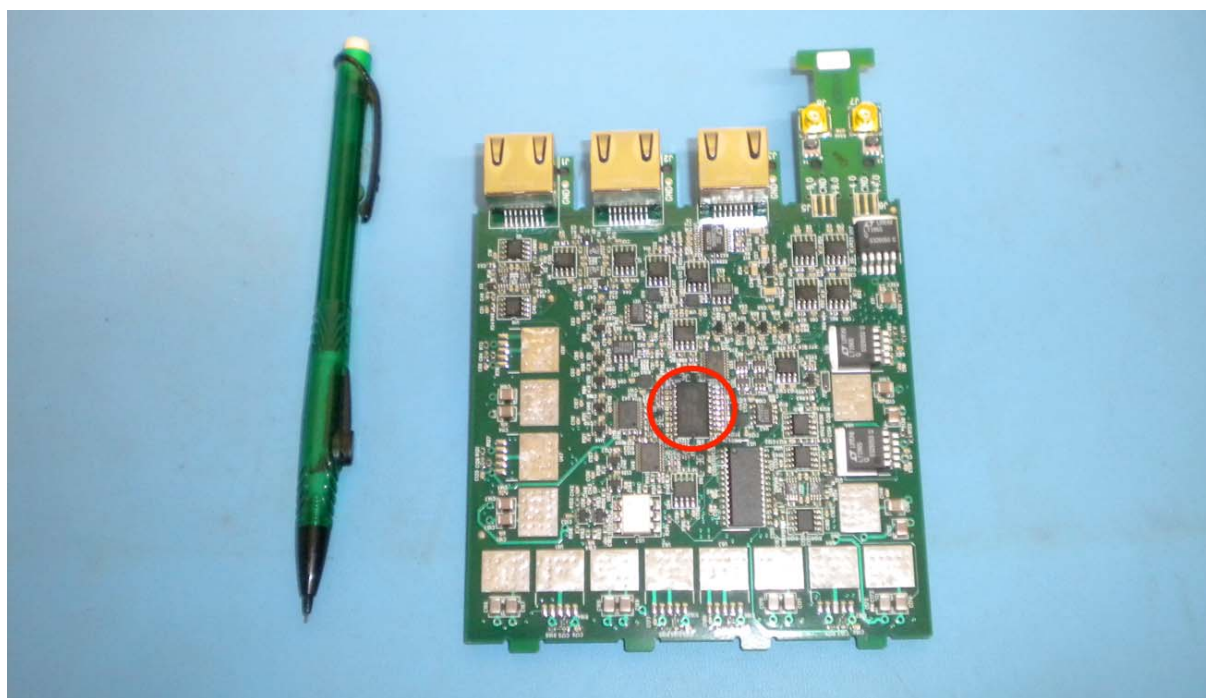


Figure 3. Photograph of the prototype AMR sensor board. The AMR sensor chip is circled.

The original plan was to use a Lyrtech multi-channel signal processing development system with 24 bit ADCs and DACs sampling at 192 kSPS that was already on hand at ESS. The unit has DSPs from Texas Instruments that provided a software configurable signal-processing platform. Although the unit was purchased in 2007, it was not used until this project began. This is when we learned that Texas Instruments would no longer support the development system. After spending a man-month of programming time on this platform, we also learned that the documentation was insufficient to develop the software we needed without technical support from Texas Instruments. DSP developers using parts from Texas Instruments traditionally purchase a support contract, but unfortunately this was not an option for our development system because it was no longer supported.

As a replacement to the Texas Instruments DSP development system, we chose to use a MOTU audio signal processing system that ESS already had on hand. This system provides 24 ADC channels and 24 DAC channels, and supports sampling rates of 96 kSPS. Audio recording

software for the MOTU system provided the ability to play predefined waveforms and record simultaneously. Although the MOTU system did not provide the ability to write a configurable closed loop feedback system in software like the DSP system, it filled the remaining functional needs. Modifications to the electronics were made as needed to test feedback circuits. The analog inputs for both signal-processing systems were AC-coupled which precluded digitizing DC signals from the sensor board. To solve this problem, special circuits were added to the development board to modulate low frequency (less than ~ 10 Hz) signals so that they could be measured with the signal processing system. CAT7 network cables were used to route the signal between the prototype sensor board and the digital audio system because these cable contain shielded twisted pairs that provide shielding to both magnetic and electric fields. This arrangement of having the audio digitizing system and analog signal processing separated by relatively lengthy cabling is not ideal from a noise perspective, but does allow construction of a low-cost prototype using existing hardware that serves as a test bed for evaluating different sensor operating modes. Photographs of the setup are shown in Figure 4.



The prototype sensor was tested by placing it in a Helmholtz coil provided by NIST (see Figure 5). A fixture was made to hold the sensor in the center of the Helmholtz coil. This coil provides a uniform magnetic field that can be controlled from the MOTU signal processing system. Python¹ scripts were written to generate waveforms that are played to the sensor board during an experiment. The Helmholtz response was calibrated using a Bartington MAG-03 flux-gate magnetometer with a factory certified calibration (the certified calibration error was 0.05%). The flux-gate calibration was verified by measuring the magnetic field produced by a the EMI transmitter coil shown in Figure 6. Using the known coil diameter, number of turns, and measured current, the field at the center of the coil was calculated and compared with the flux-gate measurement. Most of the error (6.8%) between the measurements is attributed to uncertainty in the diameter of the EMI transmitter coil and the coil current measurement rather than with the flux-gate certified calibration factor. In the tests that follow, all measurements are scaled to the magnetic field generated by the Helmholtz coil. Therefore, procedural errors withstanding, the error in the noise density measurements described below are primarily due to the uncertainties in the Helmholtz calibration described above.

¹ Python is an open source programming language with many high-quality scientific libraries.



Figure 5. Photograph of the sensor board placed in the Helmholtz coil (left) and being lowered into a triple layered magnetic shield. Photograph of the sensor and Helmholtz coil installed inside the magnetic shield (right).

Frequency-domain experiments were conducted to characterize the noise response of the prototype sensor. The Helmholtz coil was driven with a stepped-frequency sweep that was made from 1.0 Hz to 1.0 kHz using logarithmically spaced frequencies. The excitation frequencies are chosen so that no FFT spectral leakage occurs when digitizing at 96 kHz. For each frequency, the Helmholtz coil is driven to produce a magnetic field of approximately 30 nT at the sensor (the actual coil current is precisely measured by the MOTU system). At each frequency, three cycles are played and the time-domain response is recorded. No measurements are taken during the first cycle to allow any transients to die out due to the changing frequency. The FFT of the digitized time series for the last two-cycles of each frequency is calculated, and the sensor response at the excitation frequency is taken from the FFT results. The noise response is determined from the FFT spectrum resulting from the 1.0 Hz excitation, with the noise at 1.0 Hz assumed to be the average of the noise at 0.5 Hz and 2.0 Hz. The frequency-domain sensor response and noise response are calibrated by equating the sensor response at the excitation frequency to the magnetic field generated by the Helmholtz coil, which is determined from the measured coil current.

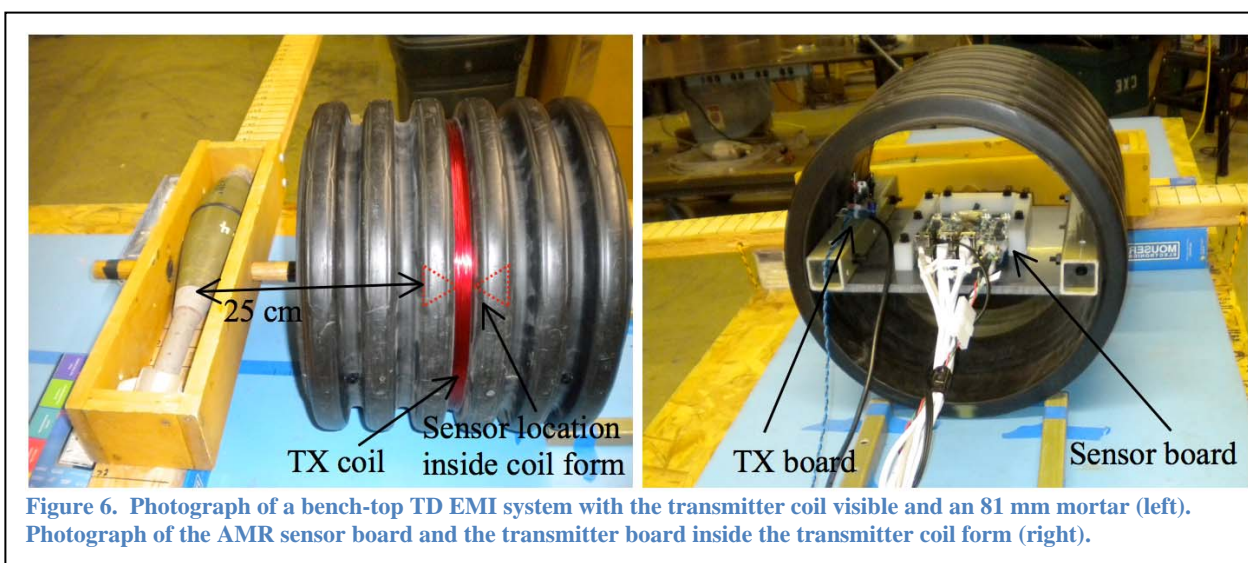
Before each experiment, the AMR sensor was poled so that the magnetic state of the sensor was aligned for proper operation and magnetic dispersion was minimized (i.e. random orientation of magnetic domains in any suboptimal direction).

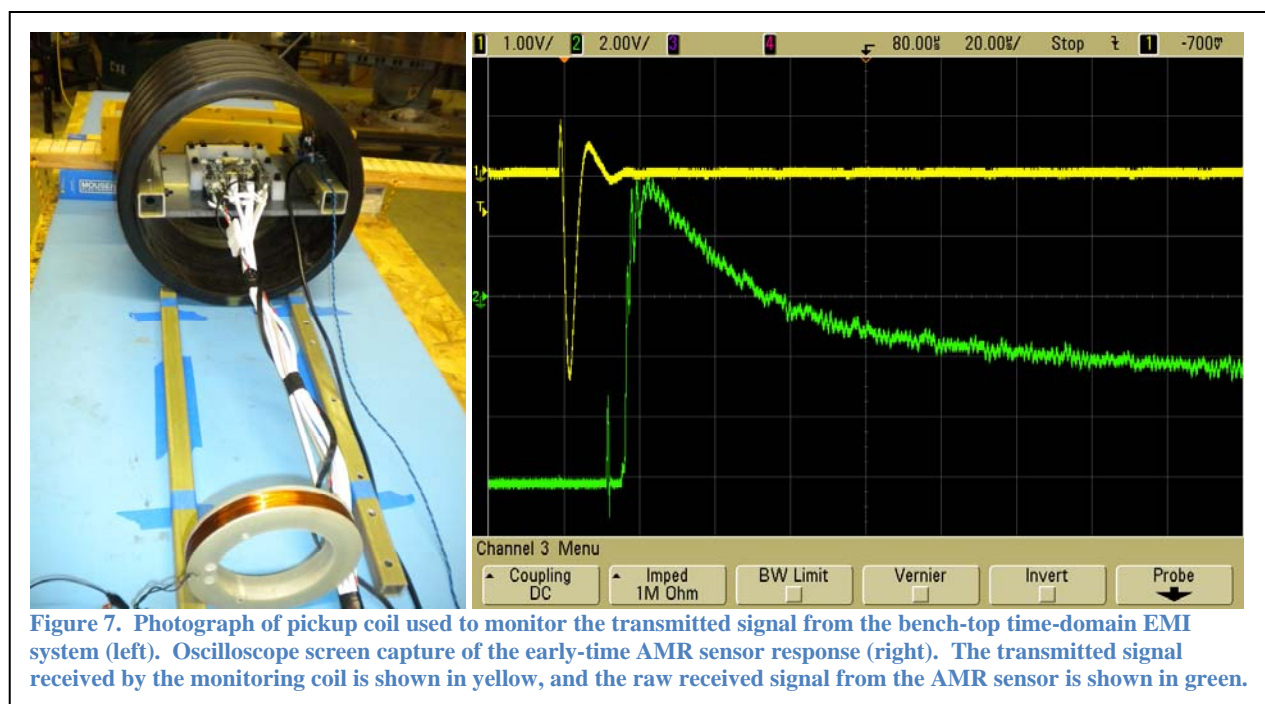
A bench-top time-domain EMI system was built to test the AMR sensor response to an actual UXO target and compare it with the response of an existing EMI system used for UXO remediation. Figure 6 shows the bench-top EMI system. The transmitter has an on-time current of 500 mA and turn-off time of about 5 μ s (see Figure 7). It generates a moment of 1.94 A-m². Table 2 lists the transmitter moments of other common EMI instruments. A more powerful transmitter can be easily constructed for field use, but is not needed for testing the performance of the MR sensor. Even this modest transmitter generates a 200 μ T field at the AMR sensor, which caused the magnetic domains in the permalloy layer to reorient. Proper sensor operation requires re-aligning these domains before making a measurement. This realignment is achieved by pulsing a current through the in-chip coils of the AMR sensor. This process takes 5-10 μ s

with the current electronics, and the system is able to record early-time signal starting at 20 μs (see Figure 7). The sensor sensitivity was reduced to 16% of maximum during EMI experiments so that very early-time measurements could be made without saturating the electronics. A sensor with improved electronics that re-aligns the permalloy magnetic domains more quickly could begin recording at 10 μs . This bench-top setup was also used to measure the passive magnetic response to a target.

Table 2. Transmitter moments of common EMI instruments.

Sensor Type	Dipole Moment	Peak Current	Turn-Off Time/Earliest Time Gate
EM61	200 A-m ²	6-8 A	216 μs time gate
EM63	1024 A-m ²	?	180 μs time gate
Zonge DNT	25 A-m ²	3 A	Depends on loop sizes
ALLTEM	693 A-m ²	11 A	200 μs minimum response time.
MetalMapper	120 A-m ²	6 A	Transmitter turn-off to 1% is on the order of 10 μs . Receiver useable 100 μs maximum after initiating transmitter turn-off.
MPV	Undertermined	2.75 A	Receiver useable 100 μs maximum after initiating transmitter turn-off.
AMR sensor prototype	2 A-m ² (design exists for ~40 A-m ²)	0.5 A (design exists for ~20 A)	< 10 μs turn-off, 20 μs time gate





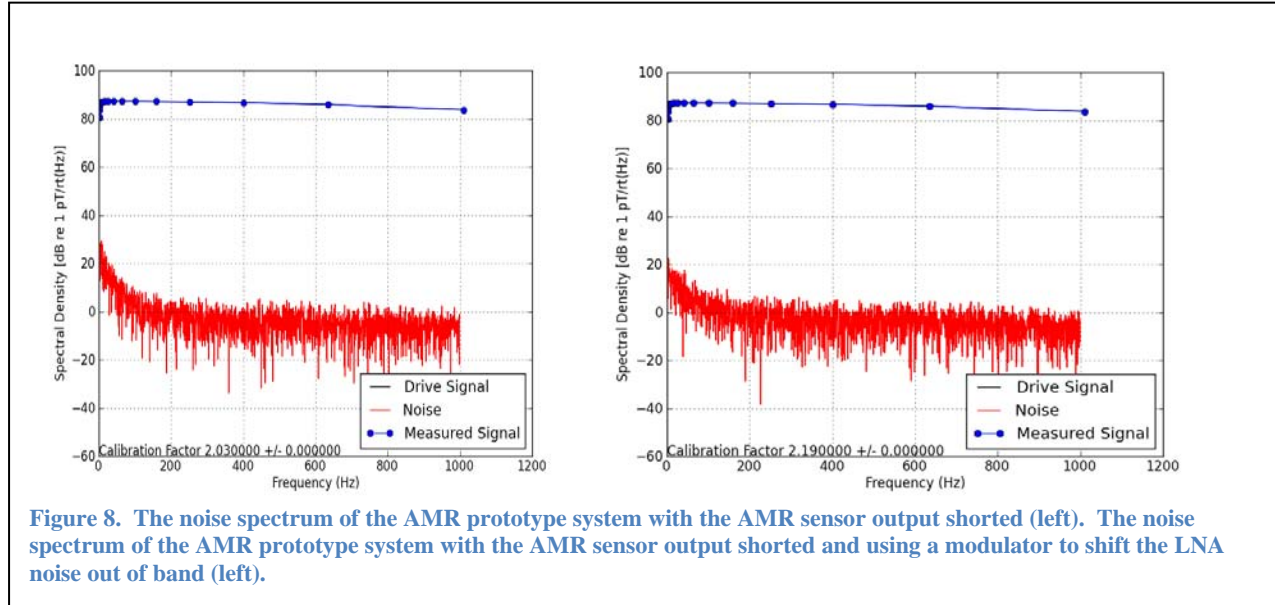
The prototype was designed to use a configurable magnetic offset to compensate for the ambient magnetic field, bridge offset voltage, thermal drift, and the unwanted EMI response of conductors in the sensor. Although this approach works, it is impractical. It produces significant power dissipation in the AMR chip due to the resistance of the offset coil, and power dissipation in the coil driver. It also causes the sensor to consume more power which is a negative attribute for battery powered instruments. Power dissipation in the AMR chip exacerbates thermal drift. To alleviate these difficulties, the prototype was modified to enable an electronic offset adjustment. At this time, the electronic offset adjustment is static, meaning that its operating point is set at the beginning of an experiment and not changed during the experiment. This setup addresses the ambient magnetic field and bridge offset compensation, but is not able to compensate for thermal drift and the unwanted EMI response of the instrument's conductors.

A frequency-domain EMI system was not built because a separate bucking coil would be needed at each receiver for each transmitter. This is impractical when more than one transmitter polarization is used. For this reason, FD EMI sensors have not been used in 'advanced' EMI sensors that have many polarization combinations of transmitters and receivers.

5 Results and Discussion

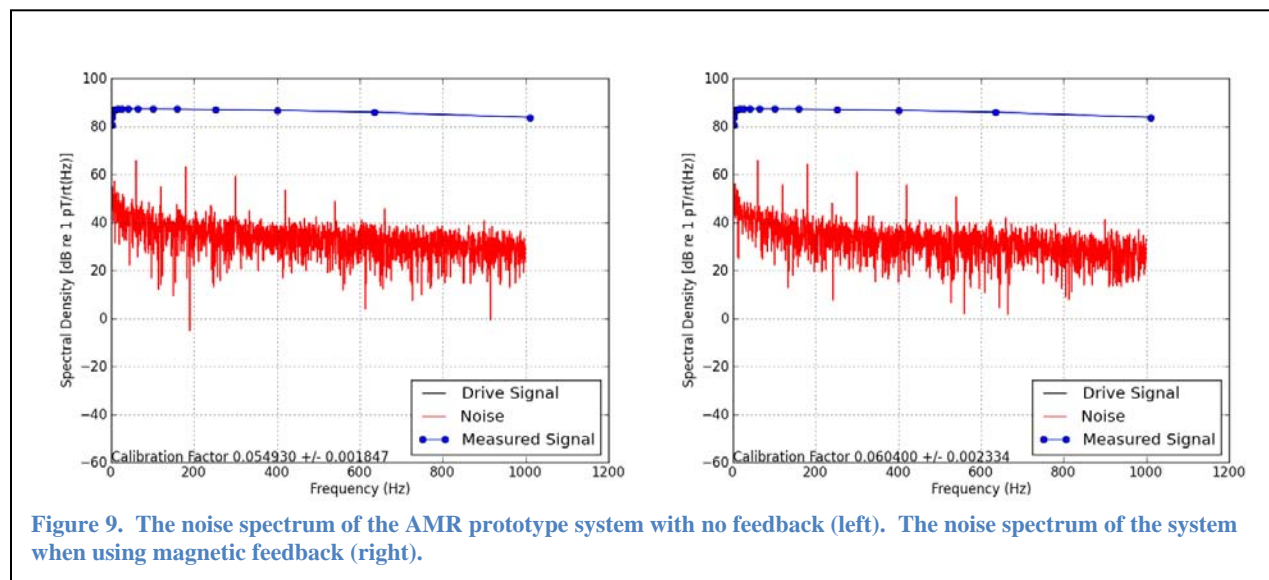
This section presents the experimental results and discusses implications of these results. Before conducting response tests of the AMR sensor, the noise of the measurement system was evaluated. The voltage output of the AMR bridge was shorted and the noise spectral density was measured as described in the Materials and Methods section. The left panel in Figure 8 shows the noise density of the system with no modulation. The right panel is the results after electronically modulating the noise out of measurement band (1 kHz). Both graphs indicate increasing fluctuation noise (i.e. 1/f noise) for frequencies less than 200 Hz. The modulation

technique does reduce the fluctuation noise. The noise density was scaled by calibrating the sensor response without the AMR bridge shorted to the known fields generated by the Helmholtz coil. Because the expected noise densities for the AMR sensor system are greater than $1 \text{ pT}/\sqrt{\text{Hz}}$ ($0 \text{ dB re } 1 \text{ pT}/\sqrt{\text{Hz}}$), the electronic and digitizing systems are quiet enough to permit testing the AMR sensor.



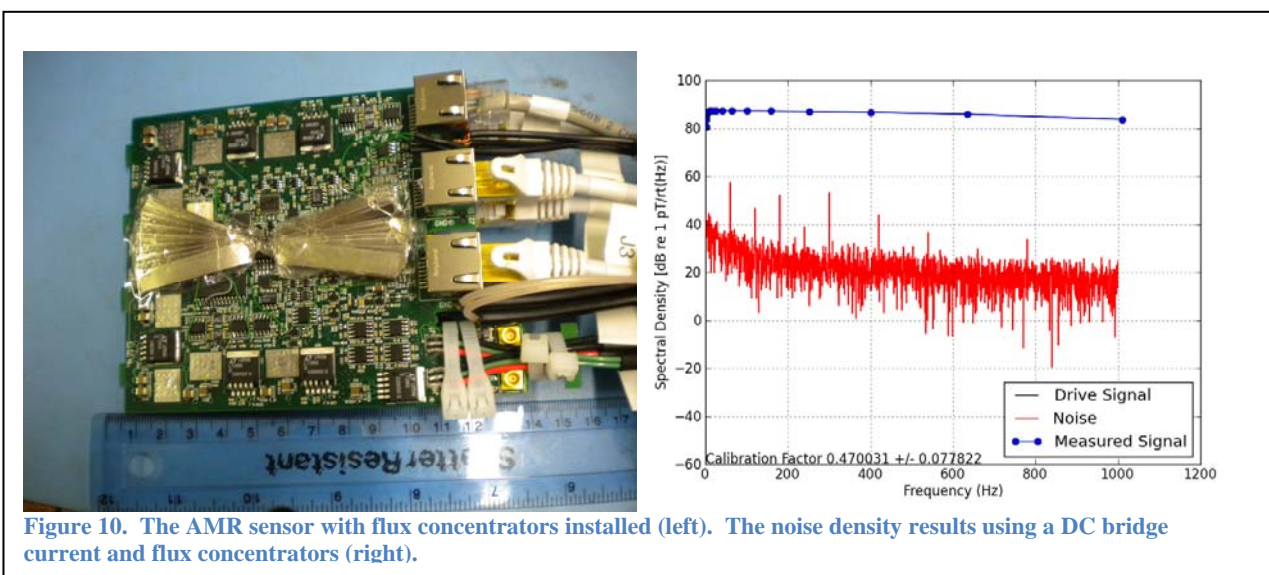
5.1 DC Biased AMR Noise Density

The noise density of the AMR sensor was tested while the bridge was energized with a DC current, and the results are shown in Figure 9. A stepped frequency sweep was conducted to determine the frequency-dependent system response so that the noise spectrum could be scaled properly. The average noise density for this configuration is about $30 \text{ dB re } 1 \text{ pT}/\sqrt{\text{Hz}}$ (i.e. $31.6 \text{ pT}/\sqrt{\text{Hz}}$) for frequencies above 200 Hz when using a 10 V bridge excitation. Stutzki et al. (2005) measured the noise density of the HMC1001 to be about $100 \text{ pT}/\sqrt{\text{Hz}}$ using a 1.2 V bridge excitation. The Stutzki results suggest that using a 10 V bridge drive would reduce the noise density to about $12 \text{ pT}/\sqrt{\text{Hz}}$, but this result does not include any noise contribution from electronics. The spikes on the noise spectra are harmonics from the 60 Hz power distribution system. Placing the AMR sensor inside the magnetic shield had little effect on these spikes. Presumably, most of the power line harmonics are induced on the cabling between the AMR sensor board and the digitizing system (i.e. the MOTU unit). Although using feedback improves the dynamic range and linearity of the system (linearity was not specifically tested), it produces a negligible improvement in the noise response.



5.2 DC Biased AMR Noise Density Using a Flux Concentrator

The noise density of the AMR sensor was tested while the bridge was energized with a DC current and a flux concentrator. The flux concentrator focuses more of the magnetic flux in the neighborhood of the sensor through the permalloy film. The concentrators were made from 3.75 x 1.25 cm Metglas film strips. The alloy film was cut into strips and stacked to a fan-shaped bundle about 1.5 mm thick (about 100 sheets). A Metglas bundle was placed on each side of the sensor chip as shown in Figure 10. The resulting noise density is 10 pT/ $\sqrt{\text{Hz}}$ (20 dB re 1 pT/ $\sqrt{\text{Hz}}$) at 500 Hz. The Metglas flux concentrators can be easily fabricated at low cost. It is likely that smaller flux concentrators can be made that provide a similar amount of gain. Liou (2008) has experimented with many flux concentrators that are about half as big as those built for this project and yield similar gains, but to date he has not yet experimented with Metglas (Liou, 2011).



5.3 AC Biased AMR Noise Density Using a Flux Concentrator

The noise density of the AMR sensor was tested while the bridge was energized with an AC current. The AC bias provides a mixer effect that modulates, shifts, or up-converts the signal to a higher frequency. When down-conversion is done, the signal is shifted to base band and the noise is shifted out of the base band. There are two contributions to sensor noise, electronic noise (Johnson noise, shot noise, and flicker) and magnetic noise (predominately flicker). The setup is able to modulate electronic noise out of band, but not magnetic noise. The up-conversion/down-conversion process adds noise. It is not possible to implement a magnetic mixer effect using the sensor because a signal on the AMR sensor bias coil only adds a signal, not multiplies, which is needed for up-conversion.

A stepped frequency sweep was conducted to determine the frequency-dependent system response so that the noise spectrum could be scaled properly. The results are shown in Figure 11. The noise density at 1 kHz is about 5.6 pT/ $\sqrt{\text{Hz}}$ (15 dB re 1 pT/ $\sqrt{\text{Hz}}$).

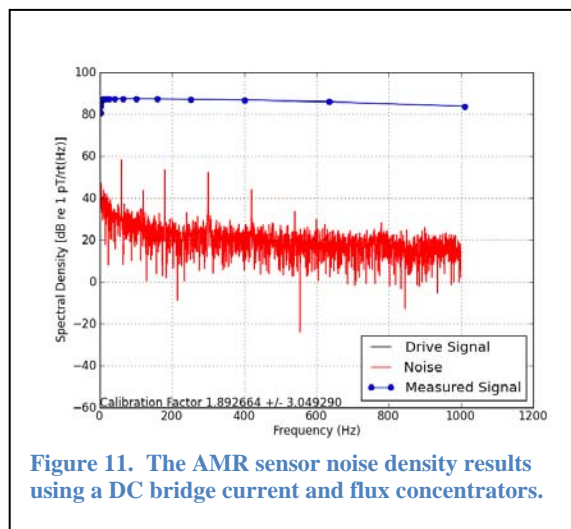


Figure 11. The AMR sensor noise density results using a DC bridge current and flux concentrators.

5.4 Issues with Flux Concentrators

The flux concentrators were made from a Metglas alloy. Metglas is a high permeability ferrous metal that is cooled from a melt at over a million degrees per second to produce an amorphous solid material. This virtually eliminates the formation of metallic crystals and large magnetic domains. Magnetic domains typically change shape and polarity due to temperature changes, mechanical shock, and history of the applied magnetic field. Subsequently, flux concentrators have historically been a poor choice when used for precision magnetometer instruments. The amorphous structure of metglas virtually alleviates these difficulties.

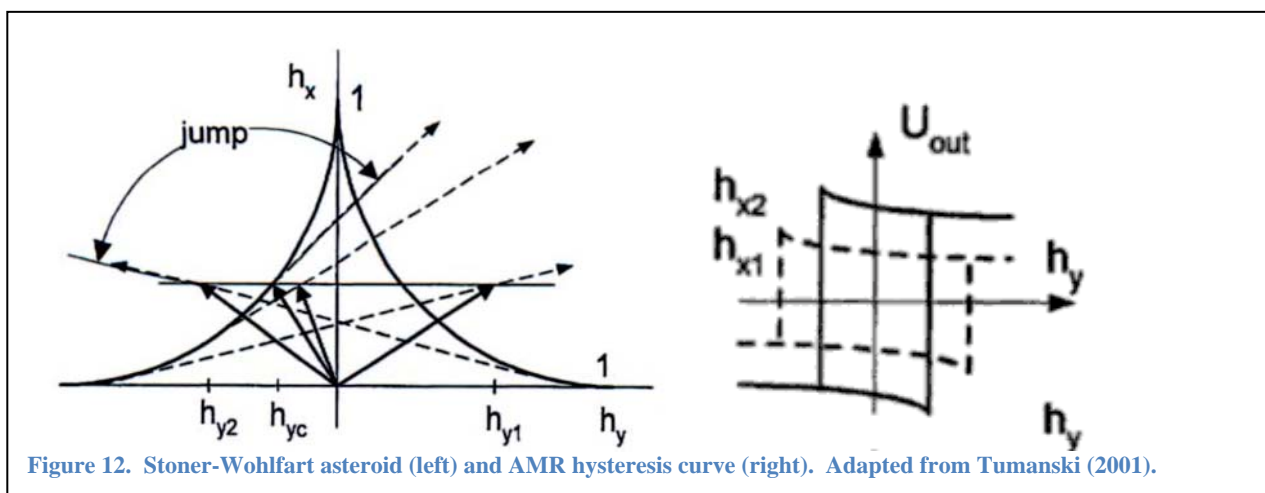
This project did not investigate multiple shapes of flux concentrators. However, gains in the range of 20 to 30 are readily achievable (Liu, 2008). The first and only flux concentrator design implemented during this project was sufficient to obtain the noise density goal for this project (less than 10 pT/ $\sqrt{\text{Hz}}$). Smith et al. (1991) found using that concentrators with a unity aspect ratio provided a gain of 20 and attenuated cross fields by 10 fold. The maximum amplification achieved by a flux concentrator with MR devices is when the thickness of the concentrator equals the gap (Drljaca et al., 2002). Flux concentrators can saturate which limits their useful maximum range in field strength. The concentrator material used for this project is an amorphous Metglas material that saturates at about 0.5 T.

5.5 Advanced Magnetic Biasing Techniques

One of the initial ideas for this project was to implement the 'reverse' biased method (Tumanski, 2001). Theoretically, this method can produce infinite sensitivity, but it requires setting the magnetization in the permalloy film in the 'hard' direction near the point where the

magnetization jumps to a new value. This is illustrated by the Stoner-Wohlfart asteroid in Figure 12 where the magnetization direction is a line tangent to the asteroid. When the tangent line approaches vertical the sensor becomes most sensitive, but small changes in the magnetic field could cause the magnetization state to flip to a much different direction. The right side of Figure 12 shows the sensor response for different bias points on the Stoner-Wohlfart asteroid. As horizontal portions of the hysteresis curve approach the vertical sections, the slope increases and the sensor sensitivity increases. The envisioned operating mode is to first operate the sensor in a low sensitivity configuration to determine the bias fields needed to rotate the permalloy magnetization near its most sensitive configuration, but not at the most sensitive point where a magnetization state transition would push the sensor out of the sensitive operating region.

The ‘easy’ direction of the permalloy film is facilitated by both material anisotropy and shape anisotropy. The sum of the material anisotropy and shape anisotropy fields in the AMR are 8 Oe (640 A/m) for the HMC1002. To get an 8 Oe bias field, this requires ~800 mA of current and 2 V of drive compliance. The HMC1002 IC package was not designed to dissipate nearly 2 W of power continuously. While this method is promising, it is not an option for the MHC1001/MHC1002 sensors unless external coils are used.



5.6 EMI Response to an 81 mm UXO

Experiments were conducted to measure the time-domain (TD) EMI response to an 81 mm UXO. Figure 6 shows the layout of the experiment. The field situation where the EMI instrument is located above the target has been horizontally reproduced on a bench top. Both the transmitter and receiver are polarized in the z-axis (depth) direction. The mortar was placed at a zero degree inclination at a depth of 25 cm below the bottom extent of the sensor (29 cm below the center of the AMR sensor). The target was moved along the x-axis (horizontal) in 3 cm increments to simulate sweeping the EMI instrument over a target. When making EMI measurements, the sensor was operated at 16% of maximum sensitivity, so the noise floor was about an six times larger than optimal. This was necessary to keep the response within the dynamic range of the sensor during the early-time transients. Ideally, the sensitivity would be adjusted during the transient decay, but this was not possible with the prototype system. The result is that late-time measurements have about six times more noise than the data that could be

recorded with an optimal system. Furthermore, the MOTU recording system employs a high pass filter with a cut-off frequency of a few Hertz. This filter causes some late-time distortion of the EMI measurements.

An 81 mm mortar was chosen as the target (see Figure 13) because it has both ferrous and non-ferrous components. Figure 14 shows the response to an 81 mm mortar as measured by the USGS ALLTEM system using an indoor test stand (Asch, 2011). The ALLTEM system uses a one meter square transmit coil, and the receiver is two opposing one meter square coils separated by a meter. The transmitter is located midway between the receiver coils, so the primary fields cancel (approximately). The uppermost receiver coil is far enough from the target that it contributes little to the target response. The large coils spread the target anomaly over 1.5 to 2.0 meters. The ALLTEM excitation is a triangle wave (the integral of a square wave) and the receivers are dB/dt sensors. The integral and derivative operations cancel, and the response of this system is equivalent to a system with a square wave excitation and B field receivers such as the AMR system built for this project.



Figure 13. Photograph of an 81mm mortar.

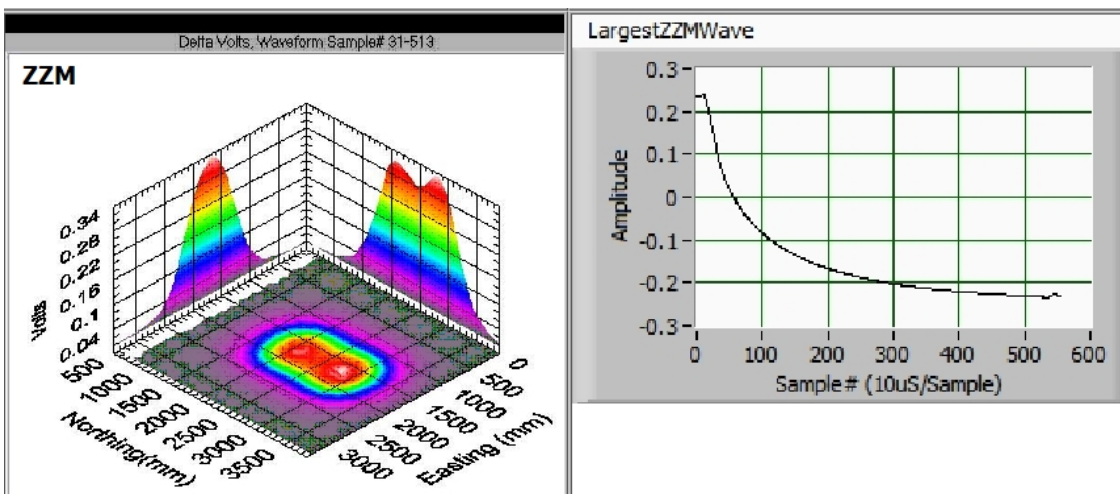


Figure 14. ALLTEM profile data for an 81 mm target at 310 μ s. The target was 44.4 cm below the ALLTEM sensor cube. Adapted from Asch (2011).

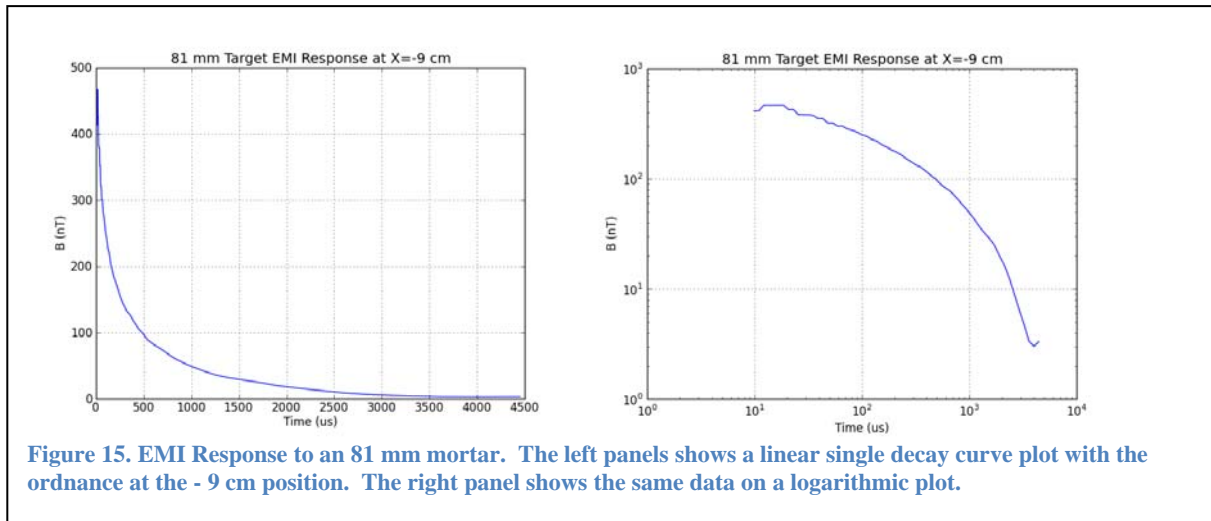


Figure 15. EMI Response to an 81 mm mortar. The left panels shows a linear single decay curve plot with the ordnance at the - 9 cm position. The right panel shows the same data on a logarithmic plot.

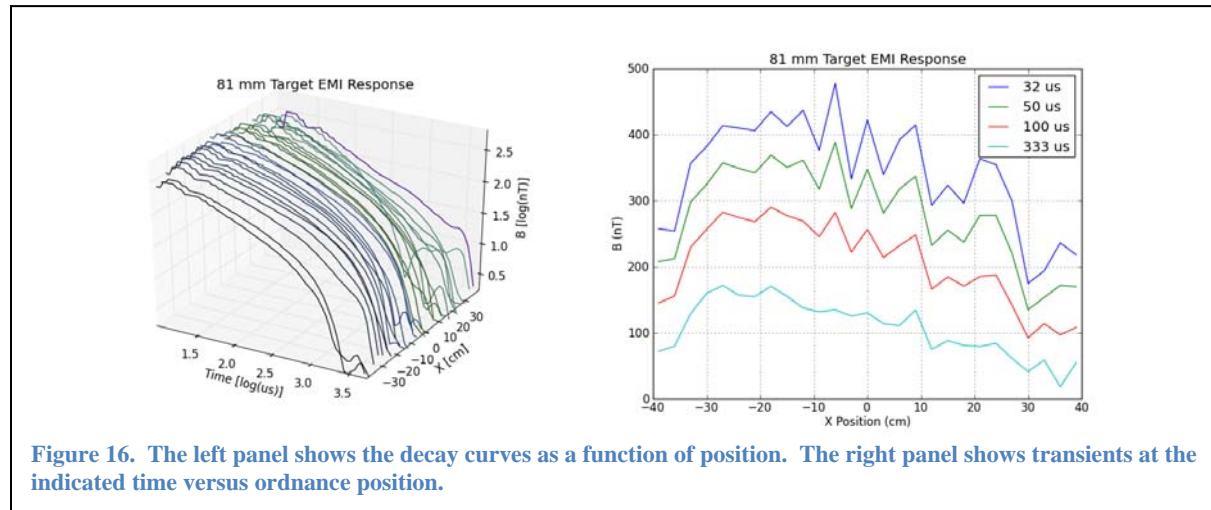


Figure 16. The left panel shows the decay curves as a function of position. The right panel shows transients at the indicated time versus ordnance position.

The TD EMI response from the AMR system is shown in Figure 15 and Figure 16. The transmitter operated at 100 Hz with an on-time and off-time of 5 ms. The MOTU system sampled the sensor waveforms at 96 kSPS (10.41666 μs). The MOTU anti-alias filter caused some ringing near the discontinuities at transmitter turn-on and turn-off times. As a result, the analyzable transient length was reduced to 4.6 ms. The following steps were made to create the time-domain decay curves, which is a procedure that would be applied to field data.

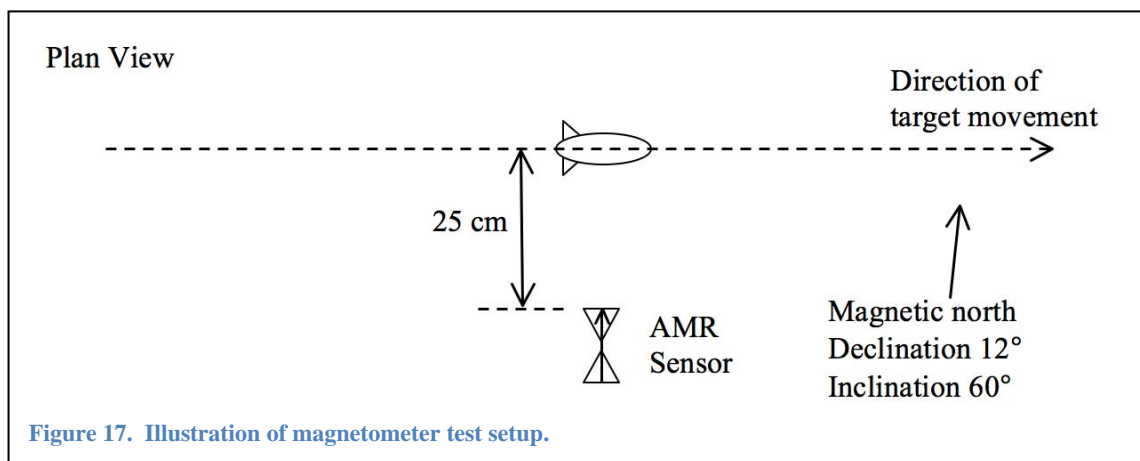
1. Ten transmitter half-cycle periods from the data recorded when the target was in place were averaged into a single half-cycle target waveform.
2. Ten transmitter half-cycle periods from the data recorded when no target was in place were averaged into a single half-cycle background waveform.
3. The background waveform was subtracted from the target waveform.
4. An array of 59 time gates (or windows) were distributed over the half-cycle waveform. The length of each gate was calculated so that it was 10% of the gate's

center time. The last gate was 45 samples (469 μ s) long, and the preceding gate lengths decreased geometrically based on the gate time. The first 12 time gates are only one sample long because the ADC sample rate was insufficient to follow the 10% length rule for early time gates.

5. The average value of the half-cycle waveforms in each time gate was calculated to produce the decay waveforms shown in Figure 15 and Figure 16.

The initial part of the decay curves shown in Figure 15 and Figure 16 is blocky because the ADC sample rate was insufficient to follow the 10% gate length rule for the first 12 time gates. The expected noise level for the last time gate when using a sensor with a noise density of 6 pT/ $\sqrt{\text{Hz}}$ is 0.56 nT (accounting for 10 stacks, the sensor operating at 16% of maximum sensitivity, and a time gate bandwidth of 2.2 kHz). Most of the decay curves in Figure 16 appear noise free down to at one nT, but some have noise levels as large as a few nT. This may be due to cultural noise or sensor drift. An attempt to remove 60 Hz harmonics did not appreciably improve the data.

Figure 16 shows the target response as a function of position. A possible explanation for the choppiness seen in the response curves on the right side of Figure 16 is sensor drift. The target response data and the background response data were taken at different times, but within a few minutes of each other. Drift in the sensor baseline between target and background recordings causes uncertainty in the actual baseline value and may add unwanted choppiness in the EMI response versus position. A solution to this problem is to make precise baseline measurements that account for drift as described in the Sensor Calibration and Drift section below. Although accounting for drift is impractical with the current electronics, the next generation electronics design will account and compensate for drift. In Figure 16 it is noteworthy that the early-time and late-time curves for positions less than 0 cm show similar anomalies, but in the -20 to -30 cm interval the anomaly does not persist into late-time. This is expected because the ferrous main body is closest to the EMI sensor for positions less than zero and the aluminum tail is closest for positions greater than zero. The induced eddy currents in the non-ferrous portion of the target will decay more quickly than the currents in the ferrous body. It is also noteworthy that the target anomaly from the AMR system spans about 80 cm and that the ALLTEM anomaly spans 1.5 – 2.0 meters due to its large induction coils. The improved spatial resolution of the AMR system will provide more detailed datasets that aid classification routines.



5.7 Magnetometer Response to an 81 mm UXO

An experiment to measure the magnetometer response to an 81 mm UXO was performed. The experiment configuration was identical to the TD EMI experiment using a 25 cm offset (see Figure 17). At each target position, both the background DC magnetic field and the field due to the target were measured using a DC voltmeter connected to the LNA output. Figure 18 shows the magnetic field anomaly produced by the target after subtracting the background field as measured with the AMR sensor and a Bartington Mag-03 flux-gate magnetometer. The AMR amplitude response was calibrated using the factory calibrated response from the flux-gate. The AMR curve has a small amount of noise due to uncompensated drift in the sensor response (explained below). Because the anomalous fields from passive magnetic measurements exhibit only one-way attenuation with distance from the target rather than two-way attenuation suffered by EMI measurements, passive magnetic surveys are able to detect ferrous bodies at a further distance than EMI measurements. Consequently, the magnetic anomaly is broader than the EMI anomaly shown in Figure 16. This large target produces a magnetic anomaly is nearly 60 dB above the sensor's noise floor for one second measurements. These measurements were taken at 16% of the AMR sensor's maximum sensitivity. After increasing the sensitivity to 100%, it was possible to observe the 81 mm target response when it was two meters from the sensor.

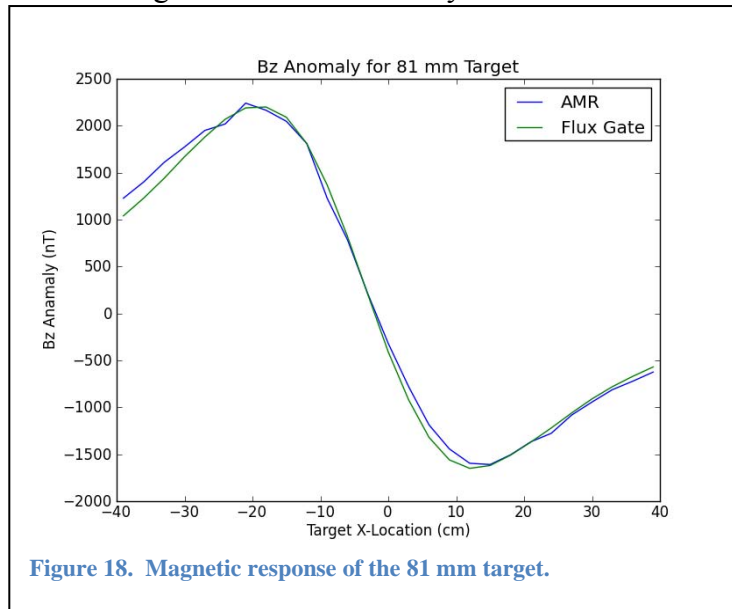


Figure 18. Magnetic response of the 81 mm target.

5.8 Response to a 25 mm Target

A small piece of steel rod (25 mm diameter 104 mm long) was used as a proxy to measure the response to 20 mm targets using the same setup as used for the 81 mm target. A photograph of the 25 mm target is shown in Figure 19, and Figure 20 shows its decay curves. The passive magnetic measurements after background subtraction are also noted on these graphs. Note that the x-oriented target has a longer decay time than that of the z-oriented target as expected. The z-oriented target has a larger magnetic response than the x-oriented target as expected (the magnetic declination was about 10 degrees off of the Z-axis).



Figure 19. Photograph of a 25 mm target.

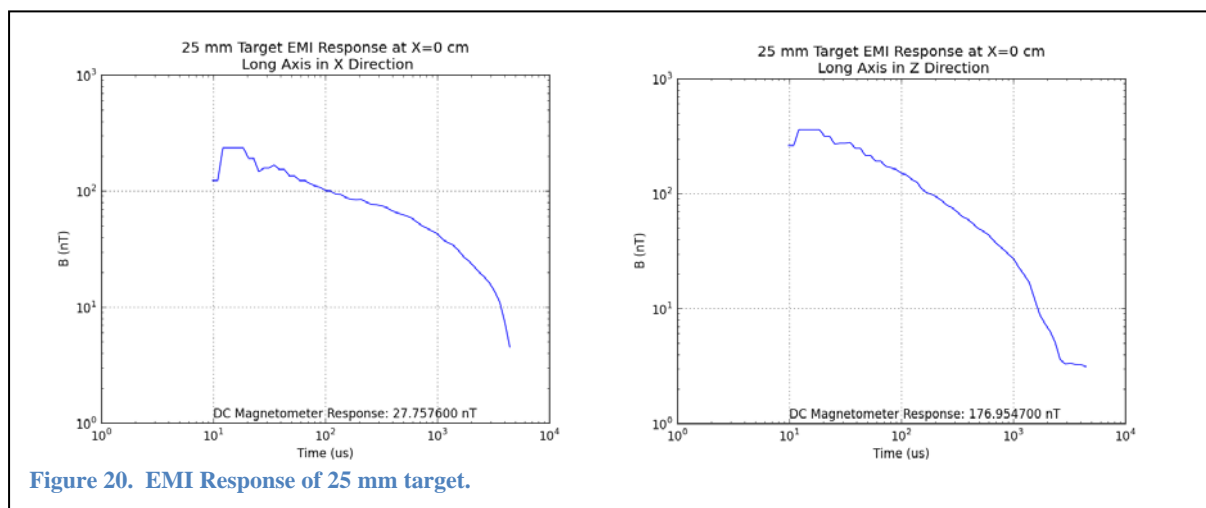


Figure 20. EMI Response of 25 mm target.

5.9 Sensor Calibration and Drift

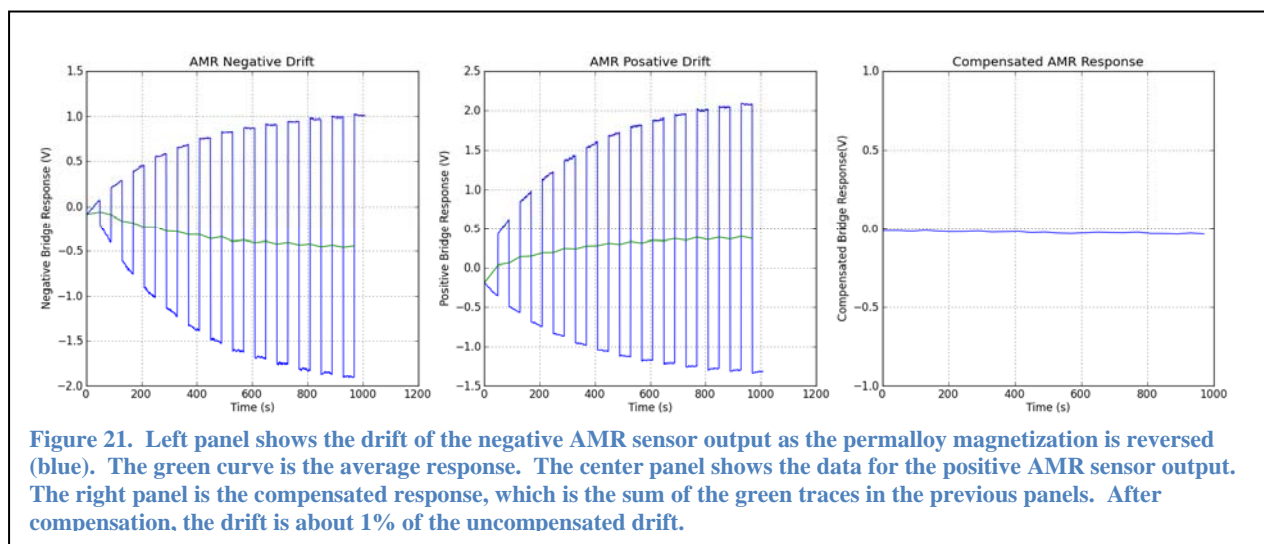
The amplitude calibration factor for the HMC1002 sensor is determined by sending a known current through the on-chip magnetic field offset coil. Determining the offset calibration factor requires more effort. The offset response of the sensor is due to offset voltages generated by the electronic circuitry, and most of these offsets change very little with time and temperature. The exception is bridge offset voltage, which changes with temperature. Because of the large amount of amplification applied to the bridge sensor signal, small variations in the bridge offset voltage cause large changes in the sensor's offset response. Therefore it is extremely important to account for the changing bridge offset voltage when determining the intercept calibration factor. When current flows through the AMR bridge, power is dissipated in the AMR sensor and its temperature increases causing changing offset voltages. Honeywell has addressed this problem (Honeywell, 2005) by periodically reversing the magnetization of the permalloy film to change the response due to the external magnetic field. Because the electronic offset voltage will remain the same before and after changing the magnetization direction, subtracting measurements taken before and after flipping the permalloy magnetization results in twice the magnetic response voltage. Adding these measurements results in twice the offset voltage. Once the offset voltage it known is can be compensated either electronically or digitally.

To test this drift compensation method, a time sequence was recorded where the permalloy magnetization direction was reversed every 40 seconds, and the recorded data were analyzed to determine the AMR sensor offset voltage as a function of time. The results are shown in Figure 21. In the left panel, the blue trace shows the drift of the negative AMR sensor output as the permalloy magnetization is reversed, and the green curve is the average response. The center panel shows the data for the positive AMR sensor output. The right panel is the compensated response, which is the sum of the green traces in the previous panels. After compensation, the drift is about 1% of the uncompensated drift.

The thermal drift in this prototype is much higher than it would be for a final design because a large number of inefficient linear regulators are employed in the prototype to power many circuits that are not needed in the final implementation. The hottest temperature on the board at the conclusion of the test was 72 °C as measured with an IR thermometer with most parts of the board above 60 °C. The temperature at the beginning of the test was 25 °C. It was difficult to

specifically determine the temperature of the AMR chip because it was mostly covered with hot melt glue for the flux concentrators.

The envelopes of the blue traces in Figure 21 are reflective of the large drift that had to be managed during the experiments made for this project. The current sensor design has an electronic nulling circuit controlled by the digital signal processing system that can be used to cancel the bridge offset voltage and/or the response to the ambient DC field. However, the MOTU signal processing system is only able to send scripted signals to the AMR sensor board, subsequently a software controlled feedback to the electronic nulling circuit is not possible. The choppiness of the results in Figure 16 would likely be reduced with proper dynamic drift compensation.



6 Conclusions and Implications for Future Research

COTS signal processing hardware (the MOTU digitizer) was used so that expedient and cost effective experiments could be conducted to investigate the AMR sensor performance. For UXO remediation efforts, these sensors enable the development of small hand-held instruments that are ideal for both detection and classification. COTS AMR sensors provide a unique combination of beneficial attributes. The following attributes are noteworthy.

1. The noise floor of the AMR sensor is sufficiently low to be used in UXO surveys. The noise floor is comparable to small search coils and flux-gate magnetometers (see Table 1).
2. The sensor can be used as a receiver in both passive magnetic surveys and active EMI surveys. Having both sensor types on the same instrument will allow both data types to be collected in one pass and reduce the survey costs.
3. EMI surveys using B field sensors do not require as much dynamic range as those using dB/dt sensors.
4. Very-early time-domain EMI data can be recorded without waiting for induced EMF to decay as with induction coil receivers. Very-early time-domain data can be

recorded when near very large transmitters. In this work, we have recorded data as early as 20 μs , and improvement on this is possible with better circuitry.

5. The EMI results were obtained with a $\sim 2 \text{ A}\cdot\text{m}^2$ transmitter with an 0.5 A driver circuit. ESS has designed an 80 $\text{A}\cdot\text{m}^2$ transmitter with a 20 A driver circuit, but to date has not built it. Most EMI instruments generate 25 to 200 $\text{A}\cdot\text{m}^2$, with smaller moments used in man-portable equipment. This larger moment will significantly increase the detection range for handheld AMR instruments.
6. A very low noise pre-amplifier circuit has been designed with the high gain and the frequency response needed for both early-time EMI measurements and DC magnetometer measurements.
7. The small size of these sensors provides the high spatial resolution needed for characterization of small targets. It also allows implementation of a multiple offset, multiple polarization receiver array in a small package.
8. The cost of these sensors is low. An entire sensor array can be fabricated on a circuit board using automated assembly methods. No manual manufacturing or assembly methods are required.
9. The small size and ruggedness of these sensors will allow them to be used on underwater platforms such as flying wings and hand-held diver equipment.
10. The HMC1002 AMR sensors can be calibrated using dedicated circuitry. For a linear calibration, the multiplier is determined by supplying a precisely known current to the AMR offset coil and measuring the response. The intercept calibration is

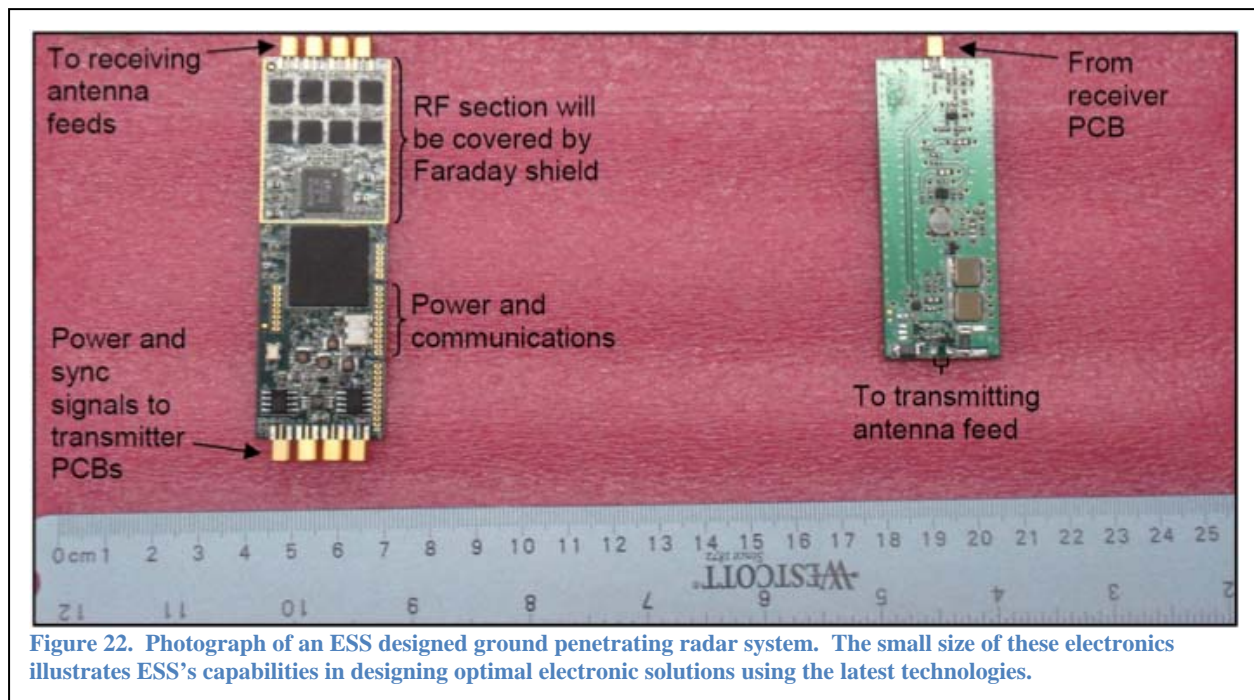


Figure 22. Photograph of an ESS designed ground penetrating radar system. The small size of these electronics illustrates ESS's capabilities in designing optimal electronic solutions using the latest technologies.

determined by reversing the magnetization in the permalloy film and subtracting the measurement results. This cancels the bridge offset.

11. Barkhausen noise is least pronounced when the permalloy film is nearly saturated. After poling, the film is saturated in the easy direction. By frequently poling the sensor, Barkhausen noise can be minimized.

Our primary recommendation for further development is to build a man-portable instrument for UXO detection and ‘advanced’ discrimination. The unique functionality of AMR sensors facilitate ‘advanced’ (i.e. multi-sensor, multi-polarization) EMI measurements in a portable instrument that can access most terrain types and navigate heavy vegetation. The envisioned man-portable instrument contains the EMI instrument, magnetometer, navigation instruments, and an acquisition PC. ESS is well versed in designing miniaturized portable instrument packages. For example, Figure 22 shows the complete set of electronics for one of our ground penetrating radar systems. Although the sensor design will be based on the current prototype, the following improvements will be made.

1. Implement a dynamic offset circuit that can be used to null the sensor, compensate for thermal drift, and compensate for the EMI transient generated by conductors in the instrument.
2. Use the dynamic offset circuit to null out the response of conductive bodies making up the instrument so that the sensitivity can be adjusted as the EMI transient decays.
3. Optimize the flux concentrator shape and minimize its size.
4. Add an efficient FPGA controlled digital signal processing system to the sensor board that simultaneously digitizes all channels.
5. This instrument would incorporate the latest cost-effective navigation technology (see the third paragraph of Section 3 for an overview of these technologies). Use a navigation package that includes GPS, inertial measurements, and stereo video cameras.
6. Consider Bluetooth or Wi-Fi for transferring data to an acquisition program running on a COTS field ruggedized PC.
7. Consider designing a system that makes several cued acquisition surveys for each target. The advantages of multiple cued surveys are that the sensor location can be determined more accurately, noise due to sensor movement in the earth’s magnetic field is eliminated, and high quality data can be taken when the dwell time is higher. Most static cued surveys acquire data for 100 to 1000 ms – a dynamic survey would have to acquire data much more quickly.

It is also recommended that future research examine methods for reducing magnetic noise. The electronic forms of noise have been addressed in this work, but magnetic noise such as Barkhausen noise has not. Modulation techniques addressing electronic noise have provided modest improvements in noise density. A modulation scheme that leverages a non-linear magnetic response would enable further improvements in noise density. For example, Edelstein et al. (2004) implemented MEMS vibrating flux concentrators to reduce magnetic noise with modulation and achieved ~ 1 pT/Hz noise density. Biasing a flux concentrator near its saturation

point may provide a similar non-linear effect without the need for a complex customized integrated circuit. This is recommended as future research.

Finally, it is possible to increase AMR sensitivity with reverse magnetic biasing of the permalloy film. Although this is not practical with the Honeywell sensors, it is recommended for future research.

7 Literature Cited

- Asch, T.H., 2011, ALLTEM Test Stand I and II Results, ESTCP Project MR-0809: U.S. Geological Survey, Denver, CO.
- Barrow, B., Khadr, N., and Bell, T., 2006, Evaluation of Laser Based Positioning for Characterization of EMI Signals from UXO, Symposium on the Application of Geophysics to Engineering and Environmental Problems, Seattle, WA, 2006, paper 176.
- Bianchi, C, and Meloni, A., 2007, Natural and Man-Made Terrestrial Electromagnetic Noise: an Outlook, *Annals of Geophysics*, v. 50, n. 3., pp. 435-445.
- Chaiken, A., 1996, Report on Demonstration Project: Imaging Detection of Unexploded Ordnance using Giant Magnetoresistive Sensor Arrays, Materials Science and Technology Division, Lawrence Livermore National Lab, Livermore, CA, UCRL-ID-125270.
- Dalichaouch, Y., Perry, A. R., Whitecotton, B. W., Moeller, C., and Czipott, P. V., 2001, Magnetoresistive Sensors for Surveillance and Remote Sensing, *Proceedings of SPIE Vol. 4232*, pp. 385-390.
- Dalichaouch, Y., Czipott, P. V., and Carin, L., 2007, Advanced Magnetic System for UXO Detection and Discrimination, Final Report, SERDP Project No. 1327, 81 p.
- Drljaca, P., Vincent, F., Besse, P., and Popovic, R., 2002, Design of Planar Magnetic Concentrators for High Sensitivity Hall Devices, *Sensors and Actuators A*, n. 97-98, p. 10-14.
- Edelstein, A.S., Fischer, G., Pulskamp, J., Pedersen, M., Bernard, W., and Cheng, S.F., 2004, Minimizing the Effect of 1/f Noise with a MEMS Flux Concentrator, *Sensors Proceeding of the IEEE*, v. 3, pp. 1562 - 1565.
- Foley, J., Mehl, R., and Lhomme, N., 2008, UXO Navigation Technology, SERDP Project, MM-1441, Final Report.
- Honeywell, 2005, Application Note – AN218, Vehicle Detection Using AMR Sensors.
- Liou, S. H., 2008, Magnetic Sensors with Picotesla Magnetic Field Sensitivity at Room Temperature, SERDP Project, M-1569, Final Report.
- Liou, S. H., 2011, Personal communication.
- Oden, C. P., Olhoeft, G. R., Jones, D. P., and Smith, S. S., 2008, Wireless Sensor Networks in Geophysics, in *Proceedings of the Symposium on the Application of Geophysics to Engineering and Environmental Problems*, Philadelphia, PA, Environmental and Engineering Geophysical Society, Denver, CO.

- Smith, N., Jeffers, F., and Freeman, J., 1991, A High Sensitivity Magnetoresistive Magnetometer, *J. Appl. Phys.*, v. 69, p. 5082-5084.
- Stutzke, N. A., Russek, S. E., Pappas, D. P., and Tondra, M., 2005, Low-Frequency Noise Measurements on Commercial Magnetoresistive Magnetic Field Sensors, *J. Applied Physics*, v. 97, 10Q107.
- Tumanski, S., 2001, *Thin-Film Magnetoresistive Sensors*, Institute of Physics Publishing, London.
- Tumanski, S., 2007, Induction Coil Sensors – a Review, *Meas. Sci. Technol.*, n. 18, R31–R46.